Chemosphere 163 (2016) 142–152

Contents lists available at ScienceDirect

Chemosphere

journal homepage: www.elsevier.com/locate/chemosphere

Mixed titanium, silicon, and aluminum oxide nanostructures as novel adsorbent for removal of rhodamine 6G and methylene blue as cationic dyes from aqueous solution

Umapada Pal [a, *], Alberto Sandoval [a], Sergio Isaac Uribe Madrid [a], Grisel Corro [b], Vivek Sharma [c], Paritosh Mohanty [c]

[a] Instituto de Física, Universidad Autónoma de Puebla, Apdo. Postal J-48, Puebla, Pue., 72570, Mexico
[b] Instituto de Ciencias, Benemérita Universidad Autónoma de Puebla, 4 sur 104, 72000, Puebla, Mexico
[c] Department of Applied Science & Engineering, Indian Institute of Technology Roorkee, Saharanpur Campus, Uttar Pradesh, 247001, India

HIGHLIGHTS

- Organic dyes are the most common pollutants in wastewater emanating from textile, paper, leather, and food industries.
- We developed mixed oxide nanoparticles of Ti, Al and Si which can adsorb cationic dyes from water efficiently.
- The adsorption efficiency of mixed oxide nanostructures containing Ti and Si are only inferior to titania nanotubes.

GRAPHICAL ABSTRACT

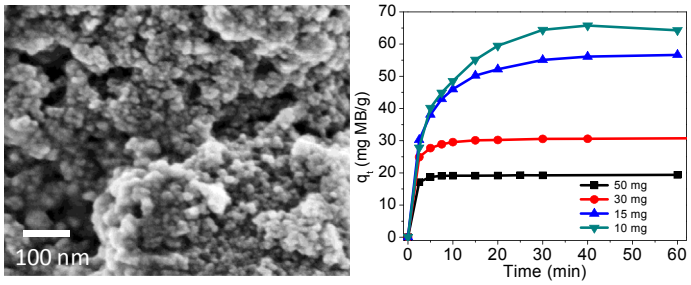

ARTICLE INFO

Article history:
Received 5 December 2015
Received in revised form
22 May 2016
Accepted 2 August 2016
Available online 13 August 2016

Handling Editor: Min Jang

Keywords:
Mixed metal oxide
Sol-gel synthesis
Mesoporous materials
Dye-adsorption

ABSTRACT

Mixed oxide nanoparticles containing Ti, Si, and Al of 8–15 nm size range were synthesized using a combined sol-gel - hydrothermal method. Effects of composition on the structure, morphology, and optical properties of the nanoparticles were studied using X-ray diffraction (XRD), scanning electron microscopy (SEM), transmission electron microscopy (TEM), microRaman spectroscopy, and diffuse reflectance spectroscopy (DRS). Dye removal abilities of the nanoparticles from aqueous solutions were tested for different cationic dyes. While all the mixed oxide nanoparticles revealed high and fast adsorption of cationic dyes, the particles containing Ti and Si turned out to be the best. The adsorption kinetics and equilibrium adsorption behavior of the adsorbate - adsorbent systems could be well described by pseudo-second-order kinetics and Langmuir isotherm model, respectively. Estimated thermodynamic parameters revealed the adsorption process is spontaneous, driven mainly by the electrostatic force between the cationic dye molecules and negative charge at nanoparticle surface. Highest dye adsorption capacity (162.96 mg MB/g) of the mixed oxide nanostructures containing Ti and Si is associated to their high specific surface area, and the presence of surface Si-$O^{\delta-}$ groups, in addition to the hydroxyl groups of amorphous titania. Mixed oxide nanoparticles containing 75% Ti and 25% Si seen to be the most efficient adsorbents for removing cationic dye molecules from wastewater.

© 2016 Elsevier Ltd. All rights reserved.

* Corresponding author.
E-mail address: upal@ifuap.buap.mx (U. Pal).

http://dx.doi.org/10.1016/j.chemosphere.2016.08.020
0045-6535/© 2016 Elsevier Ltd. All rights reserved.

1. Introduction

Organic dyes are the most common pollutants in wastewater emanating from textile, paper, plastic, leather, and food industries (Messina and Schulz, 2006). These dyes, dissolved in water, are not only aesthetically displeasing, but also consume dissolved oxygen and hinder light penetration, affecting aquatic life severely. Besides, some organic dyes and their degradation products are carcinogenic and toxic (Crini, 2006; Jain et al., 2007; Salleh et al., 2011; Zhang et al., 2011). Therefore, it is essential to eliminate these dyes before the discharge of wastewater.

There exist several methods for the treatment of colored wastewater, such as sedimentation, filtration, chemical treatment, oxidation and advanced oxidation processes (AOPs), electrochemical and biological treatments, adsorption and ion exchange (Gupta and Suhas, 2009). Adsorption technology is a reliable alternative to solve water pollution problem due to its simplicity, ease of operation, high efficiency, and ability to remove wide range of adsorbate using a variety of adsorbents (Ai et al., 2011; Doğan et al., 2000; Gupta and Suhas, 2009; Li et al., 2013; Zhang et al., 2011).

While a large number of cationic, anionic and nonionic (Salle et al., 2011; Rafatullah et al., 2010) organic dyes are in industrial use, a large variety of synthetic materials such as activated carbon (Li et al., 2013; Rafatullah et al., 2010), graphene oxide (Zhang et al., 2011; Li et al., 2013), carbon nanotubes (Li et al., 2013; Zare et al., 2015; Robati, 2013), and mesoporous materials (such as alumina, silica or zeolites) (Messina and Schulz, 2006; Gupta and Suhas, 2009; Robati, 2013) have been evaluated as adsorbent. Among them, activated carbon has seen to be very efficient for cleaning wastewater. However, it presents some disadvantages like high cost and loss of adsorption efficiency after regeneration (Salleh et al., 2011). On the other hand, several non-conventional, low-cost adsorbents derived from natural products such as biosorbents, agricultural by-products, and industrial wastes (Crini, 2006; Rafatullah et al., 2010) have also been utilized for this purpose.

Among the organic dyes with industrial applications, cationic dyes are in frequent use in textile industries for coloring acrylic, wool, nylon, fibers and silk. These water-soluble dyes are also known as basic dyes as they carry a positive charge in their molecules. Most of the cationic dyes are toxic, causing harmful effects such as allergic dermatitis, skin irritation and cancer (Salleh et al., 2011) to human beings. Methylene blue (MB) is a basic dye, commonly employed for dying cotton, wood, fibers and silk (Deng et al., 2011), which can cause harmful effects such as vomiting, enhanced heart beats, diarrhea, shock, cyanosis, jaundice, quadriplegia, and tissue necrosis on human beings (Li et al., 2013). Rhodamine 6G (R-6G) is also a basic dye used to dye wool, cotton, silk and paper, where fluorescent effects are required. The rhodamine family is well known for causing harmful effects in human like irritation to the skin, eyes, and respiratory tracks (Rochat et al., 1978). Drinking water contaminated with rhodamine can lead to subcutaneous tissue borne sarcoma, which is highly carcinogenic (Jain et al., 2007). It has also been proven that rhodamine can cause reproductive and developmental toxicity to human beings (Jain et al., 2007).

Effectiveness of any adsorption process largely depends on the physicochemical properties of the used adsorbent (Küçükosmanoğlu et al., 2006). The adsorption kinetics depend on adsorbate-adsorbent interaction and system conditions or parameters such as pH value, temperature, dye concentration, and adsorbent dose. Therefore, it is essential to evaluate the adsorption rate and understand the mechanism of adsorption for the design and fabrication of effective adsorbents and their application for wastewater treatment. Solute uptake, which determines the residence time required for completing the adsorption reaction (Yuh-Shan, 2004) is a very important parameter to be considered for the design of water treatment facilities. A good adsorbent should have large specific surface area for enhanced adsorption capacity and adsorption rate.

Using its good photocatalytic performance, TiO_2 has been widely utilized to eliminate or degrade several organic dyes through radical mediated oxidation processes (Nakata and Fujishima, 2012; Arbuj et al., 2010; Gnaser et al., 2005; Yogi et al., 2008; Natarajan et al., 2011; *Qin* et al., 2009). Taking advantage of the high specific surface area of nanostructures, recently TiO_2 and other metal oxides have been utilized extensively for dye degradation or adsroption purpose (Sarkar and Basak, 2013; Tadjarodi et al., 2013). Spherical TiO_2 nanoparticles of low size dispersion and high surface area (Pal et al., 2006) have seen to have enhanced solid-solution interface, high accessible surface area, and high mass transfer rate for organic pollutant adsorption (Nakata and Fujishima, 2012). Although TiO_2 nanoparticles manifest high photocatalytic performance (Nakata and Fujishima, 2012; Ganaser et al., 2005), they present very low adsorption capacity to some dyes (Zhao et al., 1998; Dong et al., 2012). On the other hand, mixed metal oxides containing two or more metals have seen to be effective catalysts and catalytic supports for a wide variety of organic reactions (Gawande et al., 2012). Recently they have been applied for several other promising applications such as in energy storage and conversion, taking advantage of their complex chemical compositions and the synergic effects of multiple metal species, which give rise to their remarkable electrochemical performance (Yuan et al., 2014). A few mixed metal oxides have also been utilized for organic dye capture recently. Wang et al. (2005) prepared $ZnO/TiO_2/SnO_2$ mixed metal oxides which are photocatalytically more active than pure TiO_2 and SnO_2, but slightly less active than ZnO in the degradation of methyl orange (Wang et al., 2005). However, used of these mixed oxides as dye adsorbant has not been verified. As TiO_2 presents a weak adsorption capacity for organic dyes, several attempts have been made to add a second metal oxide to improve its adsorption capacity (Dong et al., 2012; Ma et al., 2013; Yao et al., 2013; Sonar et al., 2013; Acosta-Silva et al., 2013; Guo et al., 2014).

In the present article, we report on the synthesis of mixed oxide nanoparticles containing titanium, aluminum and/or silicon in different proportions through a combined sol-gel hydrothermal method and their cationic dye adsorption behaviors. It has been shown that the addition of aluminum and/or silicon in titania nanoparticles improves their cationic dye adsorption capacity significantly. Along with the structural and optical properties of the nanoparticles, the effects of aluminum and silicon addition on their dye adsorption kinetics are presented.

2. Materials and methods

2.1. Chemicals

Titanium (IV) butoxide (TB, Aldrich 97%), aluminum-tri-sec-butoxide (ASB, Aldrich 97%), and tetraethyl orthosilicate (TEOS, Fluka 98%) were used as Ti, Al and Si precursor, respectively. Deionized (DI) water, absolute ethanol (anhydrous, J.T. Baker) and nitric acid (HNO_3, Aldrich 70%) were used as solvents. Ammonium hydroxide (NH_4OH, Fermont 28%) was used to adjust the pH of the reaction mixture. Methylene blue and rhodamine 6G (Sigma Aldrich) were used as test cationic dyes (Scheme 1, Supporting Informations). All the chemicals were of reagent grade, and used without further purification.

2.2. Synthesis of TiO_2 and mixed oxides containing Ti–Al, Ti–Si, and Ti–Al–Si

The nanoparticles of titania and mixed oxides were synthesized in two steps. First, a solution (solution A) was prepared by adding 0.015 mol of titanium butoxide in the mixture of anhydrous ethanol (12.5 mL) and HNO_3 (1.5 mL) under magnetic stirring for 6 h at room temperature. Another solution (solution B) was prepared by mixing 20 mL of anhydrous ethanol and 20 mL of DI water. The solution A was then added to the solution B under magnetic stirring. After about 30 min of magnetic stirring, adequate amount of ammonia (NH_4OH) solution was added to the mixture to adjust its pH 9.5. In the second step, the mixture prepared earlier (first step) was transferred to a Teflon-coated autoclave and a hydrothermal treatment was performed at 180 °C (heating rate of 3 °C/min) for 24 h. After the hydrothermal treatment, the sample was separated by centrifuging, washed several times with water (at least four times) and ethanol (at least two times), and dried in air at 80 °C for 8 h.

For the synthesis of the mixed oxides, aluminum and/or silicon precursors were added in the solution A in different molar ratios, maintaining total precursor content in the solution 0.015 mol.

2.3. Characterization

The crystalline phase of the nanostructured oxide samples was analyzed by X-ray diffraction (XRD) using a Bruker AXS D8 Discover diffractometer with monochromatic CuKα radiation (λ = 1.5406 Å) operating at 40 kV accelerating voltage and 40 mA filament current. The crystalline behavior and vibrational properties of the nanostructures were studied further by microRaman spectroscopy, using a HORIBA-JOBIN YVON LabRAM-HR spectrometer and the 632.8 nm emission of a He–Ne laser as excitation source. For the determination of specific surface area of the samples, their nitrogen adsorption-desorption isotherms at 77K were recorded in a Belsorp-Mini II (BEL Japan Inc.) analyzer, after degassing the samples at 200 °C for 4 h in vacuum. For the elemental analysis and morphological studies of the samples, a field emission high resolution scanning electron microscope (FE-HRSEM, Zeiss Auriga 3916) attached with a Bruker xflash 5010 series energy dispersed spectroscopy detector was utilized.

2.4. Adsorption tests

The experiments of cationic dye adsorption by the oxide nanoparticles were performed in a batch experiment. For this purpose, a cylindrical jacketed glass mini-reactor of 250 mL capacity with 50 mm of internal diameter and 120 mm of height was utilized. Typically, 50 mg of the sample was added into 100 mL of dye solution (10 ppm) under magnetic stirring in dark (inside a black box). At different intervals of time, about 4 mL of aliquot was taken out of the mixture and filtered by a reusable syringe (z268410) fitted with a nitrocellulose membrane filter of 0.22 μm pore size, to test the dye concentration in the filtered sample. The concentration of dye in the aliquot was determined by monitoring the most intense peaks in its absorption spectra using a Shimadzu UV-VIS-NIR 3100 spectrophotometer. Care has been taken to avoid the exposure of light to the aliquots during their transfer from reactor to the spectrometer chamber.

3. Results and discussion

3.1. Elemental and structure analysis

To verify the presence of Ti, Al and/or Si atoms in the synthesized samples, EDS elemental analysis was performed on them. EDS estimated molar ratios of the elements are presented in Table 1 comparing them with their nominal values (values used in preparing the reaction solutions). It can be observed that the EDS estimated molar ratios of the elements in the oxides are very close to their nominal values, indicating the effective incorporation of Al and/or Si into TiO_2.

The oxide nanostructures were further analyzed by X-ray photoelectron spectroscopy using a Thermo VG Scientific (England), Multitab 2000 X-ray photoelectron spectrometer (XPS), to estimate the surface elemental composition and chemical state of the elements in them. Although the XPS estimated composition of the mixed oxides varied significantly from their EDS estimated compositions, both the core level Si2P and Al2P emissions of the mixed oxide containing Al, Si and Ti revealed two components peaks each (sub-bands, see Fig. S1 of Supporting Informations), none of which corresponds to their elemental state. The appearance of two component bands at higher energy indicates the formation of mixed oxide along with the formation of nonstoichimetric oxide phases of the elements (Al and Si).

The crystallinity and structural characteristics of the oxide nanostructures were studied using XRD and microRaman spectroscopy techniques. XRD patterns of the as-prepared samples are presented in Fig. 1. The diffraction pattern of the as prepared TiO_2 sample revealed sharp and intense diffraction peaks at $2\theta = 25.34$, 37.92, 48.04, 54.06, 54.92, 62.76, 68.86, 70.32 and 75.22°, which correspond to the (101), (004), (200), (105), (211), (204), (116), (220) and (215) lattice planes of TiO_2 in anatase phase, respectively (JCPDS # 84-1285). After incorporating Al and/or Si, the XRD patterns of the oxide sample revealed all the characteristic diffraction peaks of anatase TiO_2. However, the Al-incorporated TiO_2 sample revealed an additional diffraction peak of low intensity at about 28.1°, which probably associated to the (110) lattice planes of rutile TiO_2 (JCPDS # 88-1172) or the (111) planes of Al_2TiO_5 (JCPDS# 74-1759). On the other hand, the diffraction pattern of the oxide sample containing Ti and Si revealed weaker diffraction peaks associated to anatase TiO_2, with higher angle peaks like (116), (220) and (215) almost disappearing. Finally, the mixed oxide nanostructures containing both Al and Si revealed well-defined lower angle diffraction peaks along with broader higher angle diffraction peaks of anatase. Additionally there appeared two very weak diffraction peaks at higher angles associated to rutile.

A comparative analysis of the XRD spectra of the samples indicates that incorporation of both Al and Si severely affects the crystallinity of TiO_2. It should be remembered that we kept the sum of the molar concentrations of Al and Si fixed in all the three mixed oxide samples. The variation of intensity and broadening of the diffraction peaks for the mixed oxide nanostructures (Fig. 1) indicate that the crystallinity of TiO_2 nanoparticles reduces more severally by the addition of Si than Al. It must be noted that there appeared no diffraction peak associated to phase pure alumina or silica in our mixed oxide samples.

To detect the presence of possible secondary oxide phase (aluminum oxide or silica) in the mixed oxide nanostructures, their microRaman spectra were recorded at room temperature in 100–1200 cm^{-1} spectral range (Fig. 2). All the samples revealed dispersion bands associated to the Raman active fundamental modes of anatase TiO_2, located at about 142 cm^{-1} (E_g - lowest frequency), 194 cm^{-1} (E_g - low frequency) 395 cm^{-1} (B_{1g}), 515 cm^{-1} (A_{1g}) and 638 cm^{-1} (E_g - high frequency) (Bersani et al., 1998a,b). The most intense lowest frequency E_g (at 142 cm^{-1}) mode presents a blue shift on the incorporation of Al or Si. However, the shift is more prominent when both Al and Si were incorporated into TiO_2. Meanwhile the bands associated to the remaining fundamental anatase modes maintain their position. The blue shift and

Table 1
EDS estimated molar ratio of the elements in the oxide samples in comparison with their nominal values.

Sample	Nominal molar ratio (Ti: Al: Si)	EDS estimated molar ratio (Ti: Al: Si)
TiO_2	(1: 0: 0)	(1: 0: 0)
Ti–Al–O	(2: 1: 0)	(2: 1.2: 0)
Ti–Si–O	(2: 0:1)	(2: 0: 1.1)
Ti–Al–Si–O	(2:0.5:0.5)	(2: 0.55: 0.66)

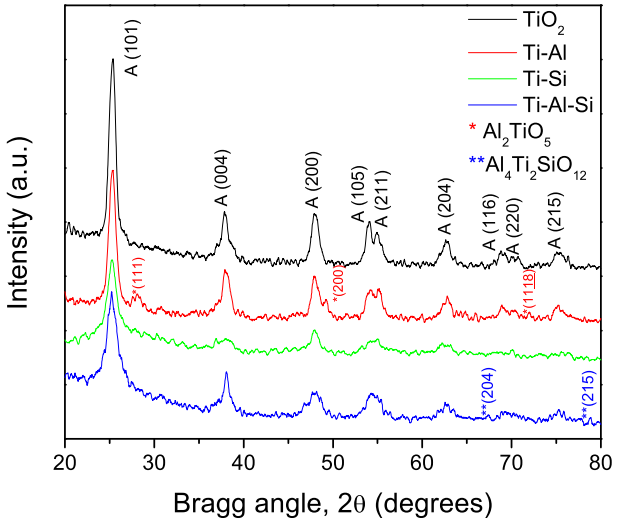

Fig. 1. XRD patterns of as prepared oxide nanostructures.

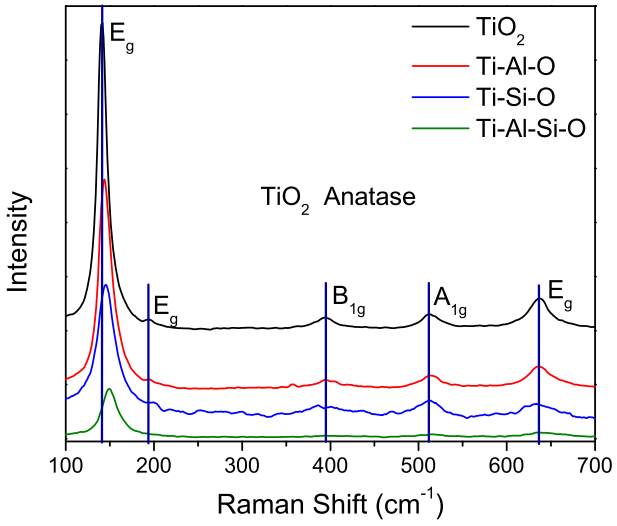

Fig. 2. Raman spectra of the as-prepared oxide nanoparticles.

broadening of the lowest frequency E_g (142 cm^{-1}) anatase mode has been reported to be due the phonon confinement, oxygen deficiencies (formation of nonstoichiometric phases) and pressure effect on the grains, induced by the surrounding grains or by the surface tension (Bersani et al., 1998a,b; Andonova et al., 2009). As has been mentioned earlier, this shift is more notable in the oxide nanoparticles containing both Al and Si. The formation on non-stoichiometric phases due to the inclusion of Al and Si atoms could be the reason for the blue shift and broadening of the lowest frequency E_g mode.

Although the incorporation of Al and/or Si in the mixed oxide samples could be confirmed from their EDS analysis, neither XRD nor microRaman analysis indicate the formation of Al_2O_3 and/or SiO_2 phase. We believe, the incorporated Si in the TiO_2 matrix remains in amorphous SiO_2 or SiO_x state, which does not produce any signature peak in XRD or Raman spectra. Similar observation has been made by Sonar et al. (2013) for their SiO_2 embedded TiO_2 nanoparticles. On the other hand, incorporated Al in TiO_2 might remain at Ti substituted lattice or at the interstitial sites. While the Ti substituted Al atoms coordinate with neighboring oxygen atoms, the interstitial Al atoms can also form its oxides in the basic ambient of the reaction solution. In fact, broadening and blue-shift of the principal E_g (lowest frequency) Raman band of the Al containing mixed oxide nanostructures indicates that Al remain in oxide state. As the formation of Al_2O_3 phase generally occurs on high temperature calcination (Liu et al., 2010; Soylu et al., 2014), its formation is improbable in our samples, as they were not annealed in air or other oxidizing atmosphere at high temperature.

The average crystallite size in the oxide nanostructures was estimated using the Scherrer equation (Cullity and Stock, 2001) to their most intense (101) diffraction peak:

$$D = k\lambda/\beta\cos\theta\,, \qquad (1)$$

where D is the average crystallite size, k a shape dependent factor usually 0.89 for spherical particles, λ is the wavelength of the X-ray (0.15406 nm), and β is the full width at half maximum (FWHM) of the diffraction peak. From the crystallite size values presented in Table 2, we can see that on incorporating Al or Si, the average crystallite size of the TiO_2 nanoparticles decreases from 18.8 nm to 11.9 nm. The crystallite size is lowest for the mixed oxide nanoparticles containing Ti and Si. As the SiO_2 and Al_2O_3 nanoparticles were in amorphous phase revealing no diffraction peak, crystallite size in them could not be estimated.

Typical SEM micrographs of the as-prepared mixed oxide nanoparticles are presented in Fig. 3. Formation of nanometer size particles of spherical shape is clear from the micrographs. Depending on their composition, the average size of the nanoparticles varied in between 14.6 and 7.2 nm. The average size of the TiO_2 nanoparticles (14.6 nm) decreased on incorporating either Al, or Si or both. The reduction of particle size (7.2 nm) is more prominent when Si was incorporated in TiO_2. Such a size reduction of TiO_2 nanoparticles on Si or Al incorporation has also been reported earlier (Sonar et al., 2013; Liu et al., 2010).

Table 2
Specific surface area and XRD estimated average grain size of the as prepared oxide nanoparticles.

Sample	BET surface area (m^2/g)	Av. Crystallite size (nm)
TiO_2	136	18.8
Ti–Al–O	157	17.1
Ti–Si–O	433	11.9
Ti–Al–Si–O	241	12.8
SiO_2	168	ND
Al_2O_3	181	ND

ND: Not defined (as the samples were amorphous).

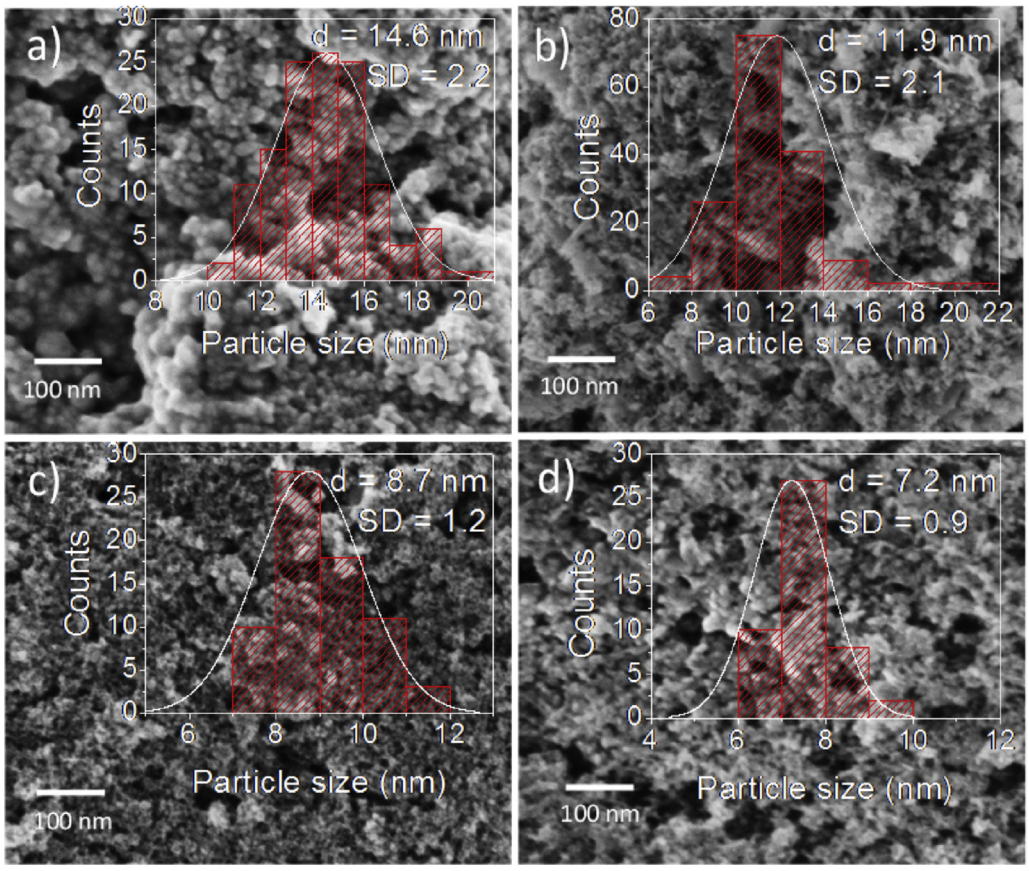

Fig. 3. Typical SEM micrographs of the oxide nanostructures containing a) only Ti, b) Ti and Al, c) Ti and Si, and d) Ti, Al, and Si.

The reduction of crystallinity of the nanostructures on incorporation of Al and/or Si is very clear from their TEM images (Fig. 4). While the low-resolution TEM images of all the samples revealed the formation of nanometer size structures, their high-resolution TEM images revealed a clear reduction of crystallinity on the incorporation of Al, Si or both in the TiO_2 matrix.

3.2. Surface area analysis

As the adsorption phenomenon takes places at the surface of adsorbents, for practical applications, adsorbents of higher surface area are preferred. The Brunauer–Emmett–Teller (BET) specific surface area of our samples estimated from their N_2 adsorption-desorption isotherms (Fig. S2, Supporting Informations) are presented in Table 2. While the pure TiO_2 revealed the lowest surface area (136 m^2/g) among the samples, its surface area increased substantially on the addition of Al or Si. The estimated specific surface area of the Al incorporated and Si incorporated oxide nanostructures were 157 m^2/g and 433 m^2/g, respectively. The highest specific surface area (433 m^2/g) of the mixed oxide nanoparticles containing Ti and Si is also reflected in the broadness of its main XRD peak (at $2\theta = 25°$, Fig. 1) associated to smaller crystallite sizes. Both the XRD and Raman spectra of the mixed oxide nanostructures indicate their partial amorphous nature. Such a reduction of crystallinity and increase of surface area of mixed oxides containing Ti, Al or Si have also been reported by several researchers (Sonar et al., 2013; Soylu et al., 2014), and associated to delayed nucleation and growth of anatase TiO_2 in presence of Al or Si.

3.3. Adsorption of methylene blue and rhodamine 6G

The methylene blue (MB) adsorption behaviors of the as-prepared oxide nanoparticles with phase contact time are shown in Fig. 5. The q_t represents the amount of adsorbed MB per gram of adsorbent (mg MB/g) calculated using the expression:

$$q_t = [(C_0\text{-}C_t)V]/M\ , \qquad (2)$$

where C_0 and C_t are the initial dye concentration and the dye concentration at time t (mg/L) in the reaction mixture, respectively; V is the volume of the dye solution, and M is the mass of the adsorbent in the reaction mixture in g.

It can be observed that the nanostructured TiO_2, Al_2O_3 and the mixed oxide containing Ti and Al do not adsorb MB until 60 min of their exposure. On the other hand, SiO_2 nanoparticles adsorb a maximum of 3.7 mg of MB/g. It has been reported that the adsorption of MB over SiO_2 is due the electrostatic attraction between the surface $Si\text{-}O^{\delta-}$ groups and the positively charged moiety of MB (Dong et al., 2012). While the partial electrical charge of the surface oxygen of metal oxides can also attract positively charged moieties of MB, the partial electrical charge of the surface oxygen of Al_2O_3 (−0.44) and TiO_2 (−0.28) are much inferior to the $Si\text{-}O^{\delta-}$ groups (−1.6) (Arai, 1996) Therefore, the adsorption of cationic dyes such as MB and R-6G at the surface of our fabricated mixed oxide nanoparticles is mainly controlled by $Si\text{-}O^{\delta-}$ surface groups. For the nanostructured mixed oxides containing Ti, Al & Si and Ti & Si, within 15 min of exposure, their adsorption capacity reaches 19 mg of MB/g, which is almost the total amount of MB present in solution, without any variation for the next 60 min, indicating the

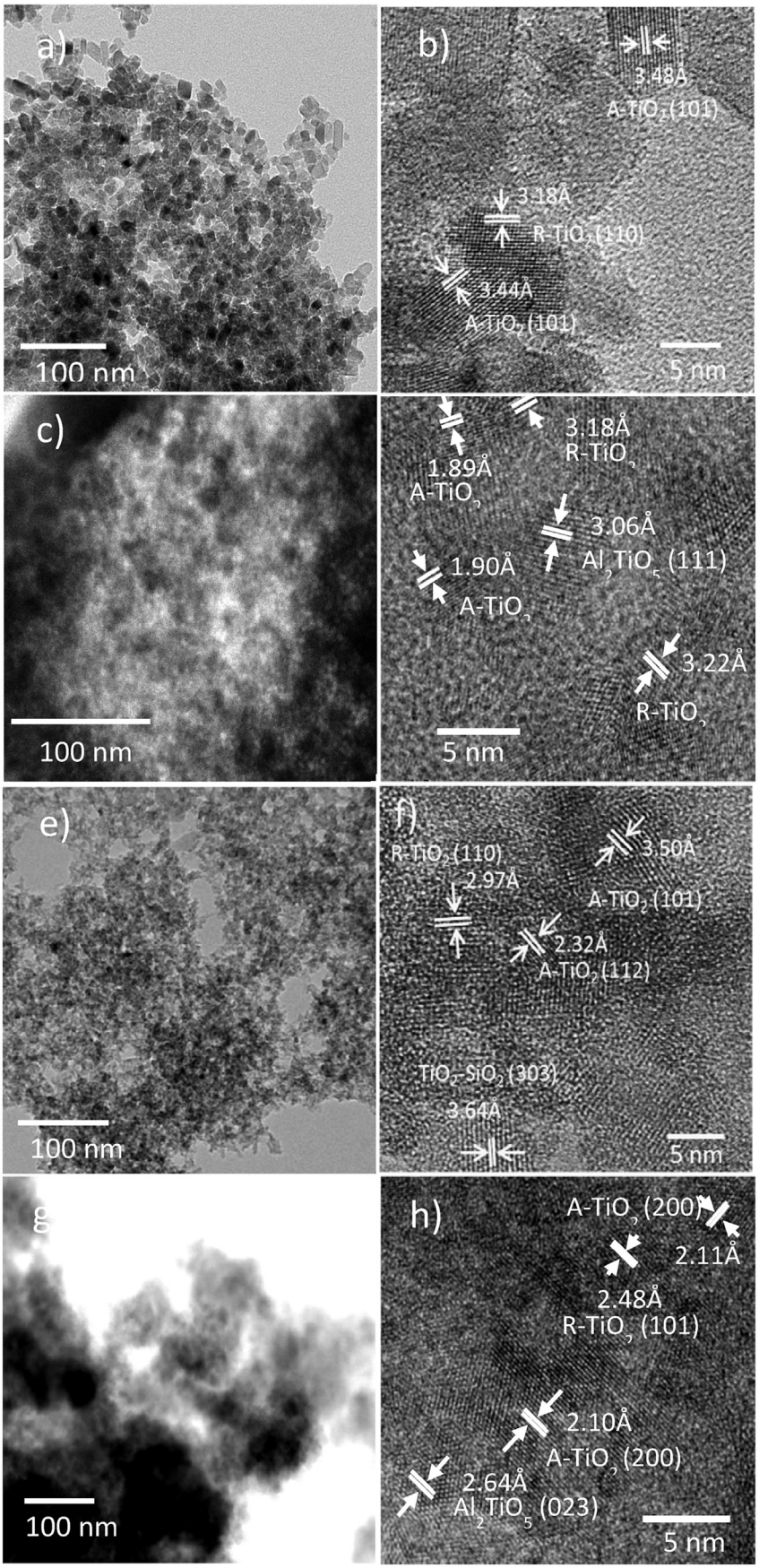

Fig. 4. Typical low- and high-resolution TEM micrographs of the oxide samples containing a, b) Ti, c, d) Ti and Al, e, f) Ti and Si, and g, h) Ti, Al and Si.

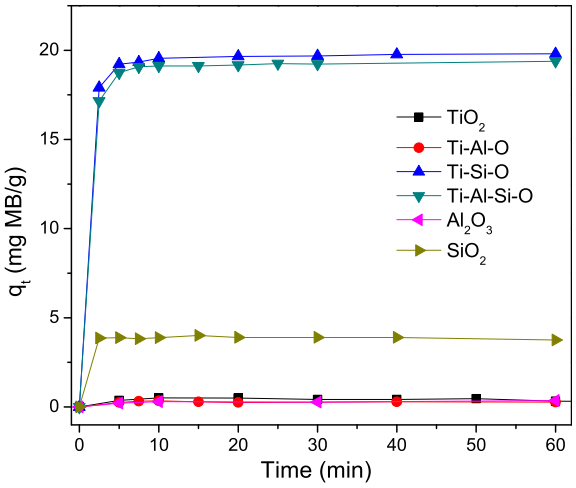

Fig. 5. MB adsorption capacity curves of pure TiO_2, Al-containing, and Si-containing mixed oxide nanoparticles as a function of time.

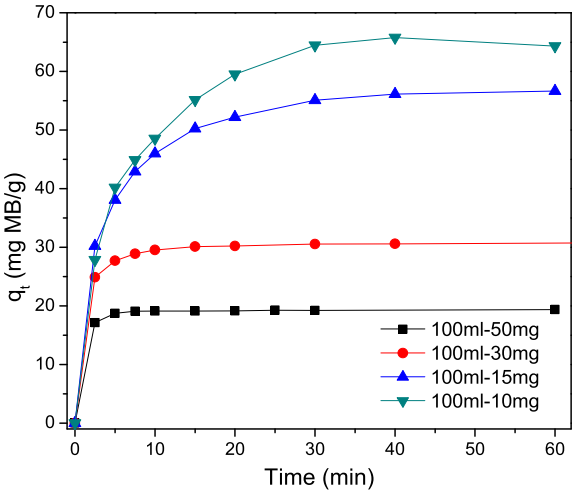

Fig. 6. Effect of adsorbent dosage on the MB adsorption capacity of mixed oxide containing Ti, Al, and Si.

enhancement of adsorption capacity of TiO_2 on incorporation of Al and Si. It has been reported that the pollutant adsorption capacity of titania is influenced by its crystal structure (Ting et al., 2014; Xie and Gao, 2009). Presence of fractional amorphous phase in titania affects the concentration of surface hydroxyl groups available for dye adsorption, and hence its pollutant adsorption capacity. In fact, the results published in literature indicate that a mixed amorphous-anatase phase titania has better adsorption capacity of MB, mainly through electrostatic attraction, in comparison with the pure anatase phase (Ting et al., 2014).

A fast and quantitative measurement of basic sites (Corro et al., 2014) at the surface of the nanostructured oxides revealed they decrease in the following order: Ti–Si–O ($6.89 \times 10^{12} g^{-1}$) ≈ Ti–Al–Si–O ($3.21 \times 10^{11} g^{-1}$) > SiO_2 ($2.36 \times 10^{10} g^{-1}$) >> TiO_2($9.46 \times 10^{9}\ g^{-1}$) ≈ Ti–Al–O ≈ Al_2O_3. This order is in agreement with the results we obtained on the adsorption capacity of our oxide nanostructures (Fig. 5); supporting the idea that MB adsorption is due electrostatic interaction between the surface charge and cationic MB molecules.

A series of experiments were performed varying adsorbent amount (50, 30, 15 and 10 mg) to compare the MB adsorption capacity of the mixed oxide nanoparticles. The adsorption capacity curves for the nanostructured mixed oxide containing Ti, Al and Si are shown in Fig. 6. It can be observed that on reducing the amount of adsorbent in the reaction mixture, the adsorption capacity at 60 min increases. The higher estimated adsorption capacity of the sample while using a lower amount of adsorbent is understandable as the adsorbent in high quantity (e.g. 50 and 30 mg) in the reaction solution adsorbs almost all the MB molecules within a very short time. Meanwhile, a smaller amount of adsorbent (e.g. 10 mg) in the reaction mixture captures MB molecules in slower rate, reaching maximum adsorption capacity in longer time. In fact, while using only 10 mg of the adsorbent (mixed oxide containing Ti, Al, and Si), the adsorption capacity reaches to its maximum after 60 min, with a value of 65.78 mg MB/g.

The same series of experiments were repeated for the nanostructured mixed oxide containing Ti and Si (Fig. 7a). As we can see, for all the adsorbent doses from 50 to 10 mg, a complete adsorption of MB reached within 30 min. The maximum adsorption capacity (162.96 mg MB/g) could be detected for 5 mg adsorbent dose, for which a complete adsorption of MB reaches in 24 h. It is very important to note that the maximum adsorption capacity of the oxide nanoparticles containing Ti, and Si (162.96 mg MB/g) is almost 2.5 times higher than the adsorption capacity of mixed oxide nanoparticles containing Ti, Al, and Si.

In the mixed oxide nanostructured containing Ti, Al and Si, the active sites for MB adsorption are the surface Si-$O^{\delta-}$ groups and hydroxyl groups of TiO_2 in amorphous phase. While Al in its elemental or oxide (Al_2O_3) form does not present any surface adsorption site for MB molecules (Fig. 5), its presence may block some of the adsorption sites of TiO_2. On the other hand, in the mixed oxide nanostructures containing Ti and Si, as there is no Al to block adsorption sites, the number of adsorption sites, especially the surface Si-$O^{\delta-}$ groups is higher (Table 1). The presence of more Si in the nanoparticles also increases the amorphous phase of TiO_2 (preventing the growth of anatase phase), resulting more adsorption sites available for MB. It has been reported that in mixed oxides, a different chemical environment of the constituting cations give rise to different reactivity towards an approaching molecule (Gawande et al., 2012). We believe, all these effects are responsible for the enhanced adsorption capacity of our mixed oxide nanoparticles containing Ti and Si.

All the samples were tested further for rhodamine 6G dye adsorption, repeating earlier experiments. As all the nanostructures revealed R-6G adsorption behaviors similar to MB, only the result of mixed oxide nanoparticles containing Ti and Si are presented (Fig. 7b). As can be seen, R-6G adsorption capacity is maximum (142.9 mg R-6G/g) for 5 mg adsorbent dose. Although this value is slightly lower than the maximum MB adsorption capacity (162.96 mg MB/g), the sample is still very good for R-6G capture from wastewater. The difference between the maximum MB and R-6G adsorption capacities of the mixed oxide nanoparticles could be due to the difference between the sizes of the dye molecules. As can be seen in Scheme 1, R-6G molecules are substantially bigger than MB molecules. The projected area of these molecules reported to be 1.34 nm^2 and 1.5 nm^2 for MB (Ardizzone et al., 1993), and R-6G (Kievsky et al., 2008), respectively.

3.4. Adsorption kinetics

The Lagergren's kinetic equations are the most commune models use to describe the adsorption in liquid-solid systems, where the adsorption clearly depends on the solid capacity (Yuh-Shan, 2004). Lagergren's pseudo-first order rate equation for a liquid-solid adsorption system is generally expressed as (Lagergren, 1898):

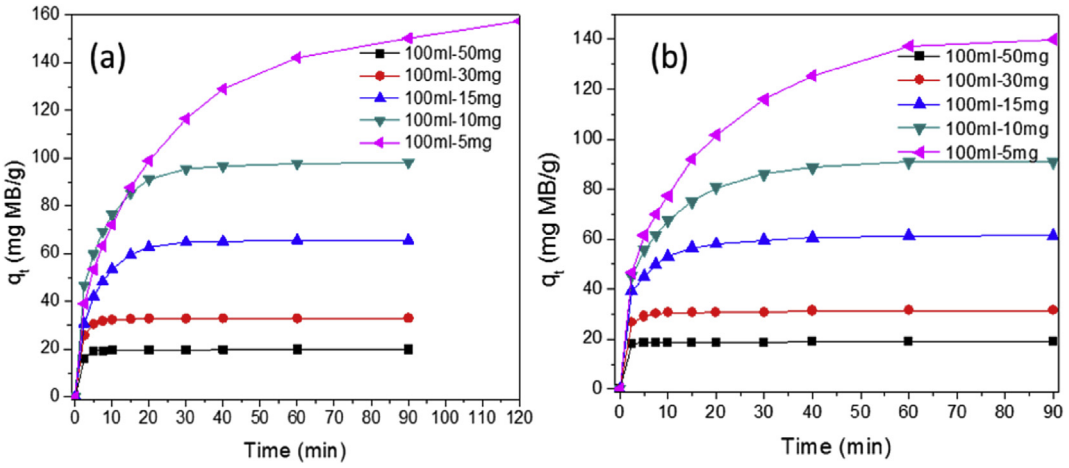

Fig. 7. Effect of adsorbent dosage on the (a) MB adsorption and (b) R-6G adsorption capacity of mixed oxide containing Ti and Si.

$$\frac{dq_t}{dt} = k_1(q_e - q_t) \tag{3}$$

where k_1 is the rate constant of pseudo-first order adsorption (min^{-1}) and q_e and q_t are the amount of dye adsorbed on adsorbent at equilibrium and at time t (mg g^{-1}); also known as adsorption capacity. Integrating Eq. (3) with boundary conditions $q_t = 0$ at $t = 0$ and $q_t = q_t$ at $t = t$, we get:

$$\log(q_e - q_t) = \log q_e - \frac{k_1}{2.303}t \tag{4}$$

The experimental adsorption data for MB over different amounts of nanostructured oxides containing Ti, Al and Si, and Ti and Si, were fitted using the Lagergren's pseudo-first order rate equation in the linear form by plotting *log* $(q_e - q_t)$ *versus* t. The slope and intercept of the linear fits (Figs. 8a and 9a) were used to determine de rate constant of pseudo-first order adsorption (k_1) and the amount of MB adsorbed per gram of adsorbent at equilibrium ($q_{e(cal)}$). The values of these constants along with their correlation coefficients (R^2) are presented in Table S1 and Table S2 (Supporting Informations) for the mixed oxides containing Ti, Al, Si, and Ti, Si, respectively. As can be noticed, the values of $q_{e(exp)}$ and $q_{e(cal)}$ estimated using the pseudo-first order equation differ significantly. In addition, the correlation coefficient values of the fits for all the adsorbent doses are not very close to one, which indicates that the pseudo-first order model does not fit with our experimental data.

The pseudo-second order kinetic model proposed by Ho and McKay (1998) is based on adsorption equilibrium capacity and the rate equation is expressed as:

$$\frac{dq_t}{dt} = k_2(q_e - q_t)^2 \tag{5}$$

where k_2 is the rate constant of pseudo-second order adsorption (g of adsorbent/mg of adsorbate/min) and q_e and q_t are the amounts of dye adsorbed on adsorbent at equilibrium, and at time t (mg g^{-1}). Integrating Eq. (5) with boundary conditions $t = 0$ to $t = t$ and $q_t = 0$ to $q_t = q_t$, we get:

$$\frac{1}{(q_e - q_t)} = \frac{1}{q_e} + k_2 t \tag{6}$$

Eq. (6) can be rearranged to obtain in linear form:

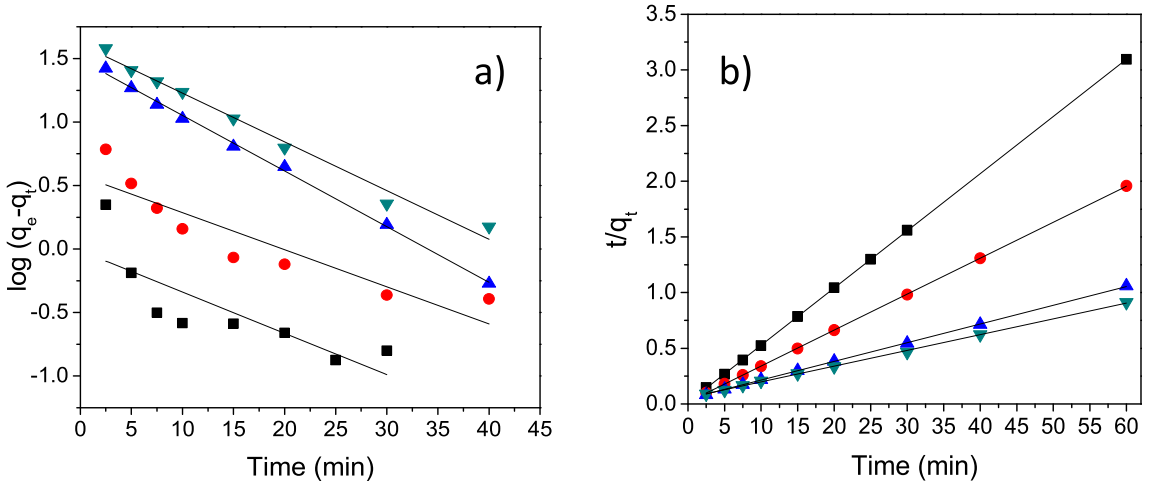

Fig. 8. (a) Lagergren's pseudo-first order and (b) Ho's pseudo-second order plots of MB adsorption, for the mixed oxide nanoparticles containing Ti, Al and Si. ■ 50 mg, ◆ 30 mg, ▲ 15 mg and ▼ 10 mg.

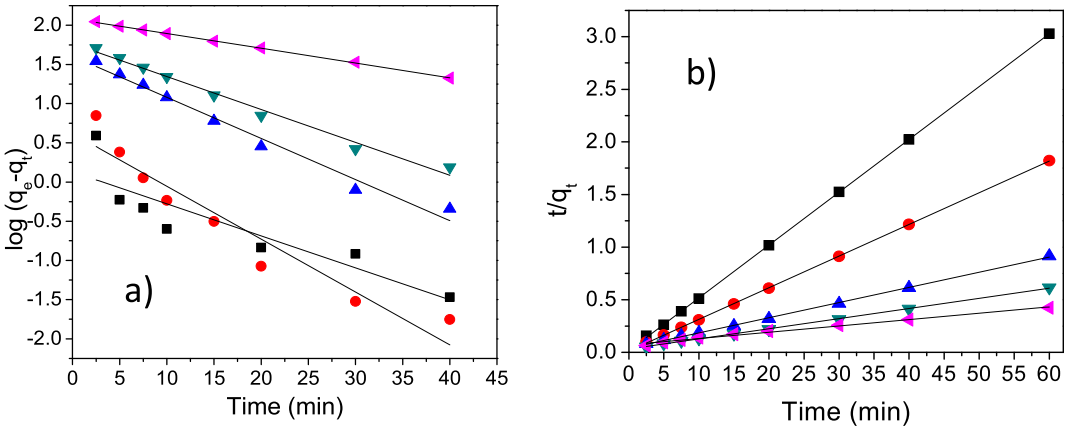

Fig. 9. (a) Lagergren's pseudo-first order and (b) Ho's pseudo-second order plots for MB adsorption by the mixed oxide containing Ti and Si. ■ 50 mg, ◆ 30 mg, ▲ 15 mg, ▼ 10 mg, and ◂ 5 mg.

$$\frac{1}{q_t} = \frac{1}{kq_e} + \frac{1}{q_e}t \tag{7}$$

The pseudo-second order adsorption constant (k_2) and the amount of MB adsorbed at equilibrium (q_e) could be estimated for the samples by fitting the Ho's pseudo-second order rate Eq. (5) plotting t/q_t *versus* t (Figs. 8b and 9b). The values are presented in Tables S1 and S2 (Supporting Informations) for the mixed oxides containing Ti, Al, Si and Ti and Si, respectively. As can be seen, the values of the correlation coefficient in these cases are very high ($R^2 \approx 1$), which indicates that the pseudo-second order model is more appropriate for describing the adsorption behaviors of all the oxide nanoparticles prepared in present work. It can also be observed that the values of $q_{e(exp)}$ and $q_{e(th)}$ obtained by the pseudo-second order model are very close.

The same methodology was used to treat the adsorption data of R-6G on the mixed oxide nanostructures containing Ti and Si. (Fig. 10 and Table S3 of Supporting Informations). In this case also, the experimental data fit better with Ho's pseudo-second model than the Lagergren's pseudo-first order model. This confirms that the adsorption of cationic dyes on the nanostructured mixed-oxide containing Ti, Al and/or Si follows Ho's pseudo-second order model.

Using the kinetic constant values obtained through Ho's pseudo-second order model, it was also possible to obtain the initial adsorption rate (mg g^{-1} min^{-1}), and the initial sorption rate ($h = k_2 q_e^2$). The values of h, presented in Figs. S1,S2,S3 of supporting information indicate that the cationic dyes are adsorbed more quickly when 50 mg of nanostructured mixed oxides were added to the dye solution; and the "speed" of adsorption decreases when the amount of adsorbent decreases. This effect can be seen in the adsorption curves, where the adsorption capacity reaches its maximum (equilibrium) more quickly (higher h values) for a higher dose of adsorbent, meanwhile it takes longer time to reach equilibrium for lower dose (smaller h values).

In Table 3, the maximum adsorption capacity of the mixed oxide nanostructures containing Ti, Al and Si, and Ti and Si are presented in comparison with the adsorption capacity values of similar mixed oxides reported in the literature. It is clear that our nanostructured mixed oxides present a competitive adsorption capacity. The adsorption capacity of the mixed oxide nanoparticles containing Ti and Si are only inferior to the adsorption capacity of titania nanotubes, when they are compared for MB adsorption.

To verify that the dye adsorption in our oxide nanoparticles is principally due to electrostatic interaction between their surface sites and ionic dye molecules, we tested the adsorption behaviors of all the nanostructures for an anionic test dye methyl orange (MO). Performing the tests in similar experimental conditions as or MB and R-6G, we found that the nanostructures do not adsorb MO.

Although the dye adsorption over metal oxide nano- or microstructures can also take place through capillary action in porous

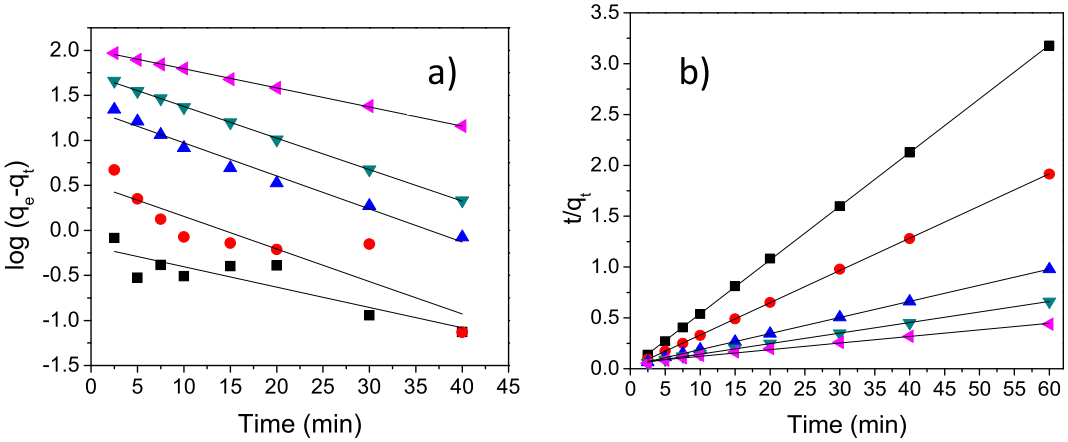

Fig. 10. (a) Lagergren's pseudo-first order and (b) Ho's pseudo-second order plots for rhodamine 6G adsorption by mixed oxide containing Ti, and Si: ■ 50 mg, ◆ 30 mg, ▲ 15 mg, ▼ 10 mg, and ◂ 5 mg.

Table 3
Comparison of MB adsorption capacity of our nanostructured mixed oxide with the adsorption capacity of other mixed oxides reported in the literature.

Material	Adsorption capacity [mg MB/g]	Conditions	Ref.
Titania nanotubes	290	At 30 °C	Hsieh et al., 2008
TX (EM science TiO_2 powder)	0.004	At 25 °C	Fetterolf et al., 2003
TiO_2 Degussa P25	0.0006	At 25 °C, pH = 6.5	Ting et al., 2014
Powder from titania layer (chemical oxidation)	0.011	At 25 °C, pH = 6.5	
$80TiO_2$–$20SiO_2$	0.0158	At 25 °C	Dong et al., 2012
TiO_2–SiO_2 composites from corn tissues	11.25–19.5	At 25 °C	Ma et al., 2013
TiO_2 – 18.6 SiO_2	22.06	At 25 °C	Yao et al., 2013
60 TiO_2 – 40 SiO_2	40	At 25 °C	Sonar et al., 2013
35 TiO_2 – DMS-1	66	At 25 °C	Acosta-Silva et al., 2013
31 TiO_2 – SiO_2	53	At 25 °C	Acosta-Silva et al., 2011
TiO_2/MSM	16	At 20 °C	Wei et al., 2011
TiO_2 – SiO_2 hollow nanospheres	73.6	At 25 °C, pH = 9	Guo et al., 2014
Mixed oxide of Ti, Al, and Si	65.78	At 25 °C	This work
Mixed oxide of Ti and Si	162.96	At 25 °C	This work

samples or at surface defect sites as has been seen in the case of titania nanotubes (Hsieh et al., 2008), we believe the effects can be summed up if we consider the concentration of Lewis sites (acid/basic) at the surface of the adsorbent. As has been presented earlier, the cationic dye adsorption capacity of the oxide nanostructures prepared in this work vary with the variation of the concentration of basic sites at their surfaces. Therefore, we believe, the contribution of electrostatic force between the adsorbent and adsorbate determines their dye adsorption capacity. In fact, the highest cationic dye adsorption capacity of our nanostructured mixed oxide containing Ti and Si is associated to the highest concentration of basic sites at their surface. Finally, the effects of solution pH and solution temperature (Figs. S3 & S4 of the Supporting Informations) on the MB adsorption capacity of the mixed oxide nanoparticles have been studied. As expected, the adsorption capacity of the sample increased gradually with the increase of solution pH and solution temperature. However, at lower pH values, the MB adsorption capacity of the sample decreases (Fig. S4, Supporting Informations). The decrease of adsorption capacity in acidic pH is due to the reduction of surface charge (negative) of the adsorbent. By monitoring the zeta potential at different pH values, the zero point of charge (zpc) for the mixed oxide was determined to be 3.2. Which indicates the mixed oxide can work as efficient adsorbent for MB and R-6G at any pH vale of the reaction mixture above 3.2.

The dye-adsorbed nanostructured adsorbents could be regenerated by treating them in a mixture of water and hydrogen peroxide (H_2O_2) in 1:2 (v/v) ratio at 50 °C for 30 min. The treatment turned the colored adsorbent nanostructures white. The nanostructures were then separated by centrifugation and dried in air at room temperature. The dye adsorption capacity of the regenerated nanostructures was tested for MB. The whole process was repeated for several times. As can be seen from Fig. S6 (Supporting Informations), the nanostructures retain more than 80% of their dye adsorption capacity on regeneration using the above mentioned process.

4. Conclusions

The sol-gel method followed by hydrothermal treatment implemented in this work produces well-dispersed nanoparticles of mixed oxides containing Ti and Al (17.15 nm average size), Ti and Si (11.89 nm average size) and Ti, Al and Si (12.78 nm average size) with high surface areas. All the as-prepared nanostructures preserve the predominant anatase phase of TiO_2. The nanostructured oxides containing Ti and Si (241 m^2/g) and Ti, Al and Si (433 m^2/g) with higher surface areas, have very high adsorption capacity for methylene blue, and both the systems follow Ho's pseudo-second order model. The highest dye adsorption capacity (162.92 mg MB/g) of the mixed oxide nanostructures containing Ti and Si is associated to their mixed amorphous-anatase phase with increased surface hydroxyl content, and the presence of surface $Si\text{-}O^{\delta-}$ groups. Presence of high negative surface charge in the mixed oxide nanostructures enhances their adsorption capacity for cationic dyes. The mixed oxide nanostructures containing Ti and Si provide a viable alternative of titania nanotubes as reusable cationic dye adsorbents.

Acknowledgments

VIEP-BUAP, CUVyTT-BUAP, CONACyT, Mexico and Department of Science and Technology (DST), India financially supported this work through the project grants # VIEP/EXC/2015, DITCo-2015-38, CB-2010/151767, and CONACyT-DST-163646, respectively. Authors are thankful to the Advance Laboratory of Electronic Nanoscopy, CINVESTAV for extending microscopic facilities for analyzing the nanostructures.

Appendix A. Supplementary data

Supplementary data related to this article can be found at http://dx.doi.org/10.1016/j.chemosphere.2016.08.020

Notes

The authors declare no competing financial interest.

References

Acosta-Silva, Y.J., Nava, R., Hernández-Morales, V., Macías-Sánchez, S.A., Pawelec, B., 2013. TiO_2/DMS-1 disordered mesoporous silica system: structural characteristics and Methylene Blue photodegradation activity. Microporous Mesoporous Mater 170, 181–188.
Acosta-Silva, Y.J., Nava, R., Hernández-Morales, V., Macías-Sánchez, S.A., Gómez-Herrera, M.L., Pawelec, B., 2011. Methylene blue photodegradation over titania-decorated SBA-15. Appl. Catal. B 110, 108–117.
Ai, L., Zhang, C., Chen, Z., 2011. Removal of Methylene Blue from aqueous solution by a solvothermal-synthesized graphene/magnetite composite. J. Hazard. Mater. 192, 1515–1524.
Andonova, S.M., Şentürk, G.S., Kayhan, E., Ozensoy, E., 2009. Nature of the Ti–Ba interactions on the BaO/TiO_2/Al_2O_3 NOx storage system. J. Phys. Chem. C 113, 11014–11026.
Arbuj, S.S., Hawaldar, R.R., Mulik, U.P., Wani, B.N., Amalnerkar, D.P., Waghmode, S.B., 2010. Preparation, characterization and photocatalytic activity of TiO_2 towards Methylene Blue degradation. Mater. Sci. Eng. B 168, 90–94.
Arai, Y., 1996. Chemistry of Powder Production, Yasuo Arai. Chapman & Hall, London, p. 68.
Ardizzone, S., Gabrielli, G., Lazzari, P., 1993. Adsorption of Methylene Blue at solid/liquid and water/air interfaces. Colloids Surf. A 76, 149–157.
Bersani, D., Antonioli, G., Lottici, P.P., Lopez, T., 1998a. Raman study of nanosized titania prepared by sol–gel route. J. Non-Cryst. Solids 232–234, 175–181.

Bersani, D., Lottici, P.P., Ding, X.-Z., 1998b. Phonon confinement effects in the Raman scattering by TiO_2 nanocrystals. Appl. Phys. Lett. 72, 73–75.
Corro, G., Bañuelos, F., Vidal, E., Cebada, S., 2014. Measurements of surface acidity of solid catalysts for free fatty acids esterification in Jatropha Curcas crude oil for biodiesel production. Fuel 115, 625–628.
Crini, G., 2006. Non-conventional low-cost adsorbents for dye removal: a review. Bioresour. Technol. 9, 1061–1085.
Cullity, B.D., Stock, S.R., 2001. Elements of X-ray Diffraction. Prentice Hall, NJ.
Doğan, M., Alkan, M., Onganer, Y., 2000. Adsorption of methylene blue from aqueous solution onto perlite. Water, Air, Soil Pollut. 120, 229–248.
Deng, H., Lu, J., Li, G., Zhang, G., Wang, X., 2011. Adsorption of Methylene Blue on adsorbent materials produced from cotton stalk. Chem. Eng. J. 172, 326–334.
Dong, W., Sun, Y., Ma, Q., Zhu, L., Hua, W., Lu, X., Zhuang, G., Zhang, S., Guo, Z., Zhao, D., 2012. Excellent photocatalytic degradation activities of ordered mesoporous anatase TiO_2–SiO_2 nanocomposites to various organic contaminants. J. Hazard. Mater. 229–230, 307–320.
Fetterolf, M.L., Patel, H.V., Jennings, J.M., 2003. Adsorption of methylene blue and acid blue 40 on titania from aqueous solution. J. Chem. Eng. Data 48, 831–835.
Gawande, M.B., Pandey, R.K., Jayaram, R.V., 2012. Role of mixed metal oxides in catalysis science-versatile applications in organic synthesis. Catal. Sci. Technol. 2, 1113–1125.
Gnaser, H., Savina, M.R., Calaway, W.F., Tripa, C.E., Veryovkin, I.V., Pellin, M.J., 2005. Photocatalytic degradation of Methylene Blue on nanocrystalline TiO_2: surface mass spectrometry of reaction intermediates. Intl. J. Mass Spectrom. 245, 61–67.
Guo, N., Liang, Y., Lan, S., Liu, L., Ji, G., Gan, S., Zou, H., Xu, X., 2014. Uniform TiO_2–SiO_2 hollow nanospheres: synthesis, characterization and enhanced adsorption–photodegradation of Azo dyes and phenol. Appl. Surf. Sci. 305, 562–574.
Gupta, V.K., Suhas, 2009. Application of low-cost adsorbents for dye removal – a review. J. Environ. Manage 90, 2313–2342.
Ho, Y.S., McKay, G., 1998. A Comparison of chemisorption kinetic models applied to pollutant removal on various sorbents. Process Saf. Environ. Prot. 76, 332–340.
Hsieh, C.-T., Fan, W.-S., Chen, W.-Y., 2008. Impact of mesoporous pore distribution on adsorption of Methylene Blue onto titania nanotubes in aqueous solution. Microporous Mesoporous Mater. 116, 677–683.
Jain, R., Mathur, M., Sikarwar, S., Mittal, A., 2007. Removal of the hazardous dye Rhodamine B through photocatalytic and adsorption treatments. J. Environ. Manage 85, 956–964.
Kievsky, Y.Y., Carey, B., Naik, S., Mangan, N., ben-Avraham, D., Sokolov, I., 2008. Dynamics of molecular diffusion of Rhodamine 6G in silica nanochannels. J. Chem. Phys. 128, 151102 (5 pages).
Küçükosmanoğlu, M., Gezici, O., Ayar, A., 2006. The adsorption behaviors of Methylene Blue and Methyl Orange in a diaminoethane sporopollenin-mediated column system. Sep. Purif. Technol. 52, 280–287.
Lagergren, S., 1898. Zur Theorie Der Sogenannten adsorption Gelöster Stoffe. K. Sven. Vetenskapsakad. Handl. 24, 1–39.
Li, Y., Du, Q., Liu, T., Peng, X., Wang, J., Sun, J., Wang, Y., Wu, S., Wang, Z., Xia, Y., Xia, L., 2013. Comparative study of Methylene Blue dye adsorption onto activated carbon, graphene oxide, and carbon nanotubes. Chem. Eng. Res. Des. 91, 361–368.
Liu, G., Yang, R., Li, M., 2010. Liquid adsorption of basic dye using silica aerogels with different textural properties. J. Non-Cryst. Solids 356, 250–257.
Liu, S., Liu, G., Feng, Q., 2010. Al-doped TiO_2 mesoporous materials: synthesis and photodegradation properties. J. Porous Mater. 17, 197–206.
Ma, H., Liu, W.-W., Zhu, S.-W., Ma, Q., Fan, Y.-S., Cheng, B.-J., 2013. Biotemplated hierarchical TiO_2–SiO_2 composites derived from Zea Mays Linn for efficient dye photodegradation. J. Porous Mater. 20, 1205–1215.
Messina, P.V., Schulz, P.C., 2006. Adsorption of reactive dyes on titania–silica mesoporous materials. J. Colloid Interface Sci. 299, 305–320.
Nakata, K., Fujishima, A., 2012. TiO_2 photocatalysis: design and applications. J. Photochem. Photobiol. C 13, 169–189.
Natarajan, T.S., Thomas, M., Natarajan, K., Bajaj, H.C., Tayade, R.J., 2011. Study on UV-LED/TiO_2 process for degradation of Rhodamine B dye. Chem. Eng. J. 169, 126–134.
Pal, M., García Serrano, J., Santiago, P., Pal, U., 2006. Size-controlled synthesis of spherical TiO_2 nanoparticles: morphology, crystallization, and phase transition. J. Phys. Chem. C 111, 96–102.
Qin, X., Jing, L., Tian, G., Qu, Y., Feng, Y., 2009. Enhanced photocatalytic activity for degrading Rhodamine B solution of commercial Degussa P25 TiO_2 and its mechanisms. J. Hazard. Mater. 172, 1168–1174.
Rafatullah, M., Sulaiman, O., Hashim, R., Ahmad, A., 2010. Adsorption of Methylene Blue on low-cost adsorbents: a review. J. Hazard. Mater. 177, 70–80.
Robati, D., 2013. Pseudo-second-order kinetic equations for modeling adsorption systems for removal of lead ions using multi-walled carbon nanotube. J. Nanostruct. Chem. 3, 55.
Rochat, J., Demenge, P., Rerat, J.C., 1978. Toxicologic study of a fluorescent tracer: rhodamine B. Toxicol. Eur. Res. 1, 23–26.
Salleh, M.A.M., Mahmoud, D.K., Karim, W.A.W.A., Idris, A., 2011. Cationic and anionic dye adsorption by agricultural solid wastes: a comprehensive review. Desalination 280, 1–13.
Sarkar, S., Basak, D., 2013. The reduction of graphene oxide by zinc powder to produce a zinc oxide-reduced graphene oxide hybrid and its superior photocatalytic activity. Chem. Phys. Lett. 561–562, 125–130.
Sonar, S., Wagh, R., Niphadkar, P., Joshi, P., Deshpande, S., Awate, S., 2013. Enhanced dual-effect of adsorption and photodegradation of SiO_2 embedded TiO_2 hybrid catalyst for improved decolourization of Methylene Blue. Water, Air, Soil Pollut. 224, 1–12.
Soylu, A.M., Polat, M., Erdogan, D.A., Say, Z., Yıldırım, C., Birer, Ö., Ozensoy, E., 2014. TiO_2–Al_2O_3 binary mixed oxide surfaces for photocatalytic NOx abatement. Appl. Surf. Sci. 318, 142–149.
Tadjarodi, A., Imani, M., Kerdari, H., 2013. Adsorption kinetics, thermodynamic studies, and high performance of CdO cauliflower-like nanostructure on the removal of Congo red from aqueous solution. J. Nanostruct. Chem. 3, 51.
Ting, H.-F., Chen, C.-M., Lu, F.-H., Suen, S.-Y., 2014. Adsorption and photodegradation of Methylene Blue using a bulk Ti material with porous titania layer prepared by chemical oxidation. J. Taiwan Inst. Chem. Eng. 45, 617–624.
Wang, C., Xu, B.-Q., Wang, X., Zhao, J., 2005. Preparation and photocatalytic activity of ZnO/TiO_2/SnO_2 mixture. J. Solid State Chem. 178, 3500–3506.
Wei, H., Cao, Y., Liu, B., Wang, X., Xu, Y., 2011. Decolration of Methyle Blue via mesoporous silica microspheres doped withTiO_2. Adv. Mater. Res. 2166, 236–238.
Xie, X., Gao, L., 2009. Effect of crystal structure on adsorption behaviors of nano-sized TiO_2 for heavy-metal cations. Curr. Appl. Phys. 9, S185–S188.
Yao, X., Zhao, C., He, R., Liu, X., 2013. Highly crystalline and silica-embedded titania rhombic shaped nanoparticles with mesoporous structure and its application in photocatalytic degradation of organic compound. Mater. Chem. Phys. 141, 705–712.
Yogi, C., Kojima, K., Wada, N., Tokumoto, H., Takai, T., Mizoguchi, T., Tamiaki, H., 2008. Photocatalytic degradation of methylene blue by TiO_2 film and Au particles-TiO_2 composite film. Thin Solid Films 516, 5881–5884.
Yuan, C., Wu, H.B., Xie, Y., Lou, X.W., 2014. Mixed transition-metal oxides:Design, synthesis, and energy-related applications. Angew. Chem. Int. Ed. 53, 1488–1504.
Yuh-Shan, H., 2004. Citation review of Lagergren Kinetic rate equation on adsorption reactions. Scientometrics 59, 171–177.
Zare, K., Gupta, V.K., Moradi, O., Salam, A., Makhlou, H., Sillanpää, M., Nadagouda, M.N., Sadegh, H., Shahryari-ghoshekandi, R., Pal, A., Wang, Z., Tyagi, I., Kazemi, M., 2015. A comparative study on the basis of adsorption capacity between CNTs and activated carbon as adsorbents for removal of noxious synthetic dyes: a review. J. Nanostruct. Chem. 5, 227–236.
Zhao, J., Wu, T., Wu, K., Oikawa, K., Hidaka, H., Serpone, N., 1998. Photoassisted degradation of dye pollutants 3. Degradation of the cationic dye Rhodamine B in aqueous anionic surfactant/TiO_2 dispersions under visible light irradiation: evidence for the need of substrate adsorption on TiO_2 particles. Environ. Sci. Technol. 32, 2394–2400.
Zhang, W., Zhou, C., Zhou, W., Lei, A., Zhang, Q., Wan, Q., Zou, B., 2011. Fast and considerable adsorption of Methylene Blue dye onto graphene oxide. Bull. Environ. Contam. Toxicol. 87, 86–90.